

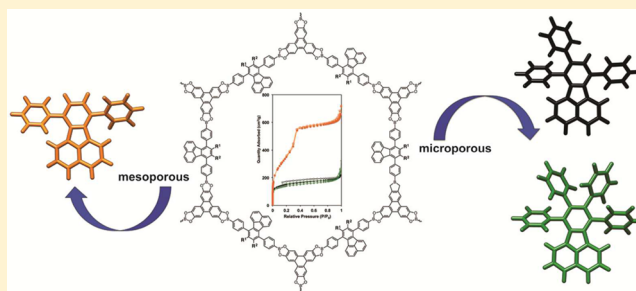
Computational and Experimental Studies on the Effects of Monomer Planarity on Covalent Organic Framework Formation

Christina M. Thompson,[†] Gino Occhialini,[†] Gregory T. McCandless, Sampath B. Alahakoon, Victoria Cameron, Steven O. Nielsen,^{*} and Ronald A. Smaldone^{*,†}

Department of Chemistry and Biochemistry, University of Texas at Dallas, 800 West Campbell Road, Richardson, Texas 75080, United States

Supporting Information

ABSTRACT: We report the synthesis of one new boronate ester-based covalent organic framework (COF) and two new covalent organic polymers (COPs) made with fluoranthene-containing monomers and hexahydroxytriphenylene. The structure of the monomer heavily influences whether this material forms a highly ordered mesoporous material (COF) or an amorphous, microporous material (COP). The synthesis of the fluoranthene monomers was carried out using a divergent strategy that allows for systematic structural variation and the ability to conduct a careful structure–function study. We found that small structural variations in the monomers dramatically affected the crystallinity, surface area, pore structure, and luminescence properties of the polymers. While each of the monomers contains the same fluoranthene core, the resultant pore sizes range from microporous (10 Å) to mesoporous (37 Å), with surface areas ranging from ~500 to 1200 m²/g. To help explain how these small structural differences can have such a large effect, we carried out a series of molecular dynamics simulations on the polymers to obtain information with atomic-scale resolution on how the monomer structure affects non-covalent COF layer stacking.



INTRODUCTION

Covalent organic frameworks¹ (COFs) are a class of crystalline porous polymers that boast high surface areas, as well as tunable pore sizes and functionalization. These attributes have led to the rapid expansion of COF-based applications including gas storage and separation,² catalysis,³ capacitive energy storage,^{2d,4} and sensing.⁵ Given the promising versatility of COFs for practical use, there have been a number of efforts to develop a clear and concise understanding of the mechanism of COF formation.⁶ Generally speaking, two fundamental processes control the structure and formation of a COF: (1) the formation of covalent bonds under thermodynamic control to form two-dimensional sheets, and (2) the aggregation of those sheets to form crystalline arrangements that result in porous frameworks. The first step of COF formation is typically achieved through the use of reversible covalent linkages such as boronic esters, imines, azines, hydrazones, and others whose reversibility can be controlled under thermal catalytic conditions. However, despite several thorough mechanistic studies on COF formation, robust design rules for the *de novo* synthesis of COFs still require further elucidation. While it has been shown that nonplanar substituents can affect COF structure,^{2f,3b,7} the extent to which out-of-plane substituents interfere with the aggregation or templation of individual sheets into a crystalline network has only been explored using a few limited structure types.

Presented here are the synthesis and polymerization of three fluoranthene (FLT)-based diboronic acid monomers containing different substituents around the periphery (Figure 1). FLT derivatives have been used in a variety of applications, including as precursors for curved polycyclic aromatic hydrocarbons⁸ and as solid-state sensors for explosive compounds.⁹ FLT derivatives are an ideal scaffold to study COF formation owing to their flat aromatic core structure and their concise and modular synthesis, which allows for the systematic evaluation of structure–function effects based on planarity, steric hindrance, and electronics. The structure of the polymers are also examined using molecular dynamics (MD) simulations which aim to explain how small differences in the monomer structure can have large effects on the microscopic polymer morphology.

RESULTS AND DISCUSSION

The synthesis of the fluoranthene-based monomers (Scheme 1) was carried out from a common cyclopentadienone precursor **1**. **1** is converted to each of the fluoranthene core structures (**2**, **5a,b**) through a Diels–Alder reaction with norbornadiene, phenylacetylene, or diphenylacetylene. Precursors **2** and **5a, b** are then converted to the corresponding diboronic acid monomers over two steps starting with a palladium-catalyzed cross-coupling reaction with bis(pinacolato)diboron. The

Received: May 30, 2017

Published: July 11, 2017

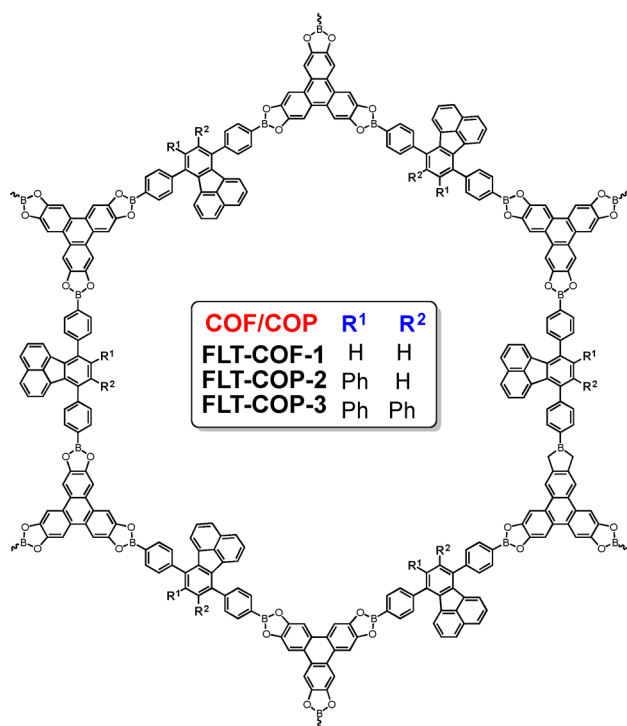


Figure 1. Structure of the FLT polymers synthesized as part of this study. The FLT materials were synthesized through a condensation copolymerization between diboronic acid monomers and hexahydroxytriphenylene, resulting in a boronate ester-based polymer.

pinacol groups are then removed through an oxidative cleavage reaction to provide the desired boronic acids. The entire synthetic route is carried out in good yields with minimal purification and can be performed on multigram scales. The copolymerization of monomers **4** or **7a, b** into COFs or covalent organic polymers (COPs) with hexahydroxytriphenylene (HHTP) was performed in a 1.5:1 molar ratio (diboronic acid:HHTP) in a mixed solvent system of mesitylene:dioxane (1:1) and heated to 90 °C for 72 h (Scheme 1). After this reaction, the insoluble powders were collected by filtration and washed with toluene before being dried under vacuum and characterized. Other reaction

conditions were tested, and the results are shown in the Supporting Information (Table S1).

The surface areas and pore size distributions were characterized by nitrogen adsorption measurements at 77 K (Figure 2). The Brunauer–Emmett–Teller (BET) surface area

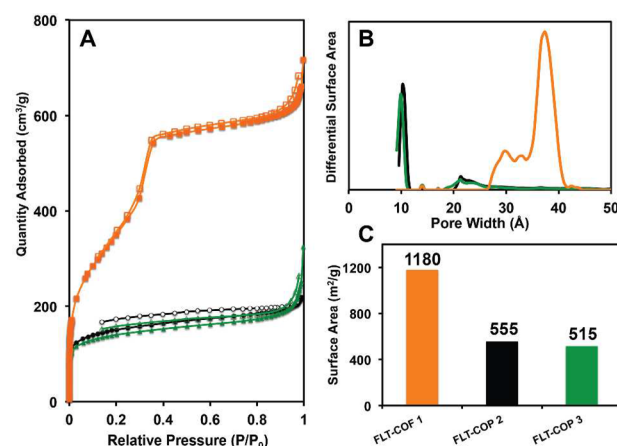


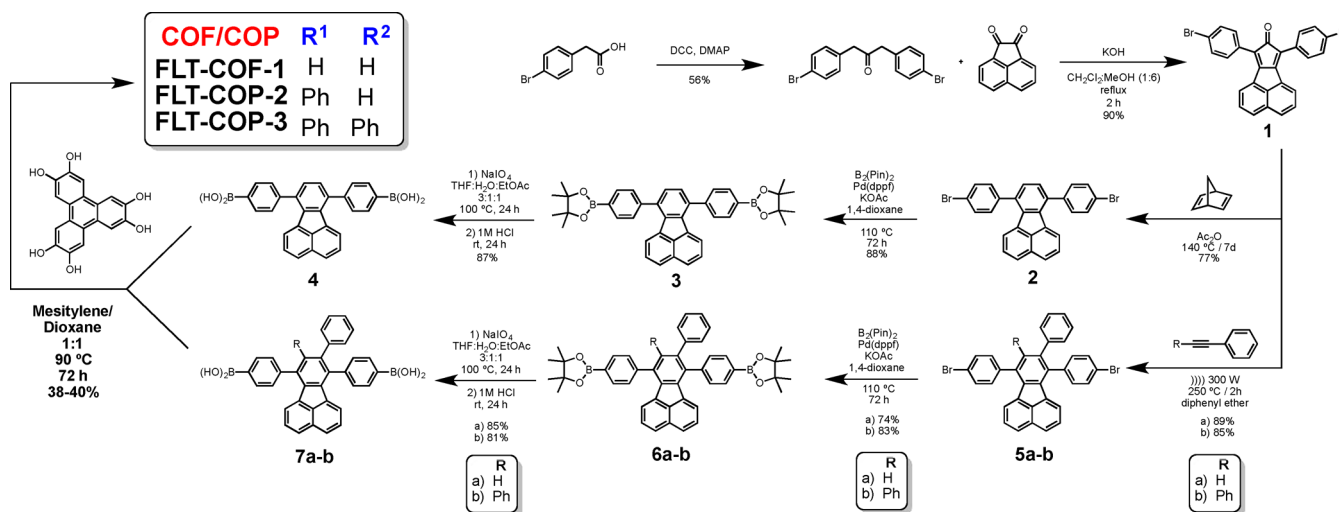
Figure 2. (A) Nitrogen sorption isotherms at 77 K for FLT-COF-1 (orange line), FLT-COP-2 (black line), and FLT-COP-3 (green line). (B) NLDFT pore size distributions for all of the FLT polymers. (C) BET surface areas for the FLT polymers.

for the FLT-COF-1 was calculated to be 1180 m²/g, while both FLT-COP-2 and FLT-COP-3 variants showed lower surface areas of 555 and 515 m²/g, respectively. Interestingly, of the three structural analogues tested, FLT-COF-1 was the only one that displayed a type IV isotherm, which is indicative of a mesoporous material. In contrast, FLT-COP-2 and -3 have type I adsorption isotherms, indicative of microporous materials.

Pore size distributions were calculated for all three polymers using the non-local density functional theory (NLDFT) method, confirming that FLT-COF-1 is largely mesoporous with pore sizes around 37 Å. FLT-COP-2 and -3 were observed to have mostly microporous character, with pore sizes of ~10 Å and a lower concentration of pores at ~20 Å.

Powder X-ray diffraction (PXRD) measurements of FLT-COF-1 showed strong diffraction, signifying a highly ordered

Scheme 1. Synthesis of FLT Monomers, FLT-COF-1, and FLT-COP-2 and -3



COF. Diffraction peaks were observed at 2.32° (100), 4.02° (110), 4.65° (200), 6.15° (210), 6.98° (300), 8.06° (220), and 26° (001) 2θ (Figure 3, top). Computational models of both

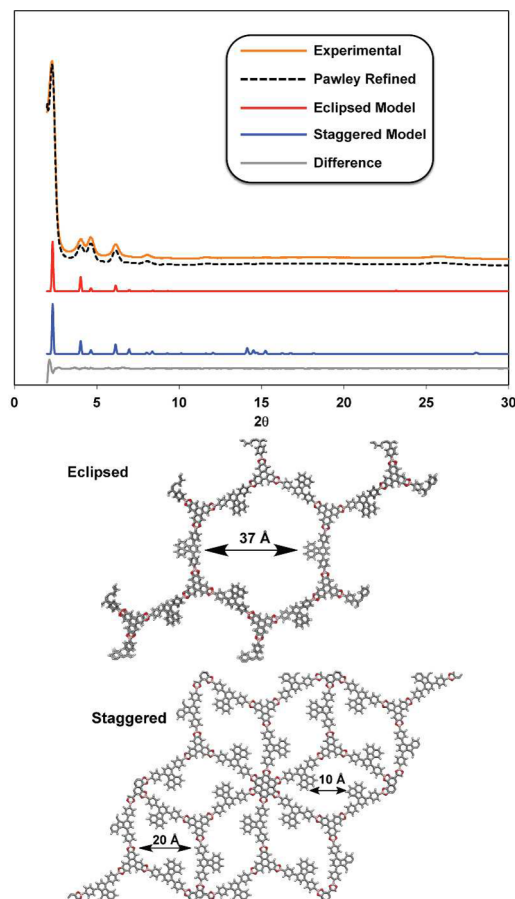


Figure 3. (Top) PXRD analysis for FLT-COF-1 including the experimental diffraction pattern (orange line), Pawley refined pattern (black dashed line), simulated diffraction pattern for the eclipsed (red line) and staggered (blue line) conformations, and the difference between the refined and experimental patterns (gray line). (Bottom) Models of the eclipsed and staggered conformations of FLT-COF-1 with annotated pore sizes.

staggered and eclipsed conformations for FLT-COF-1 were built using the gra and bnn topologies, respectively, in Materials Studio. The models were minimized using the universal force field in their respective space groups ($P3$, eclipsed, $P6_3/m$, staggered), and simulated PXRD patterns were generated (Figure 3, bottom). As expected, the simulated diffraction pattern generated from the eclipsed model resulted in the best fit. This simulation predicts a 37 Å pore size, which matches the NLDFT model of our experimental isotherm, indicating that this is likely the most accurate description of the FLT-COF-1 structure. In contrast, both FLT-COP-2 and FLT-COP-3 displayed little diffraction, indicating that, despite their moderate surface areas and microporous structures, they have poor long-range order. This is surprising, given the similarity of the chemical structures of monomers **4** and **7a,b**. Previous experimental and theoretical studies have shown that the layers of boronate ester COFs are held together through a combination of π -stacking and dipolar interactions between the lone pairs of the boronate ester oxygen atoms and the boron atoms of the adjacent layer.¹⁰ We hypothesized that the

boronate ester linkages may still be forming during the polymerization with HHTP for all three polymers, but that the steric hindrance caused by the extra phenyl rings could be disrupting either the aromatic stacking interactions between the FLT units of FLT-COP-2 and -3, or the interactions between the boron and the oxygen lone pairs. If these interactions are sufficiently hindered, the layered structure of the COF may form in two dimensions, but may aggregate in a disordered fashion as the structure-directing forces that align the COF sheets with one another are disrupted. While these simulated crystal structures are useful for correlating PXRD patterns in COFs, they are far too restrictive to provide information on how small changes in the monomer structure could potentially disrupt these important intermolecular, non-covalent interactions. This was the impetus to study these polymers using MD simulations discussed later on.

Previous reports have shown that crystalline COFs could be delaminated using certain solvent mixtures^{6a} or through self-exfoliation,¹¹ resulting in disruption of the non-covalent 3D stacking structure and loss of crystallinity while leaving the covalently linked structures intact. To explore this possibility further, we characterized each monomer and polymer using Fourier transform infrared spectroscopy (FTIR). Since there are characteristic differences¹² between the boronic acid starting materials and the boronate ester linked polymers, this technique should be able to probe the extent of boronic acid to boronic ester conversion. We hypothesized that the lower surface areas and crystallinity of FLT-COP-2 and FLT-COP-3 could potentially be explained by the presence of either poorly ordered impurities such as oligomeric boronate esters or unreacted starting materials. Shown in Figure 4 are the FTIR spectra of all three polymers and their starting materials **4** and

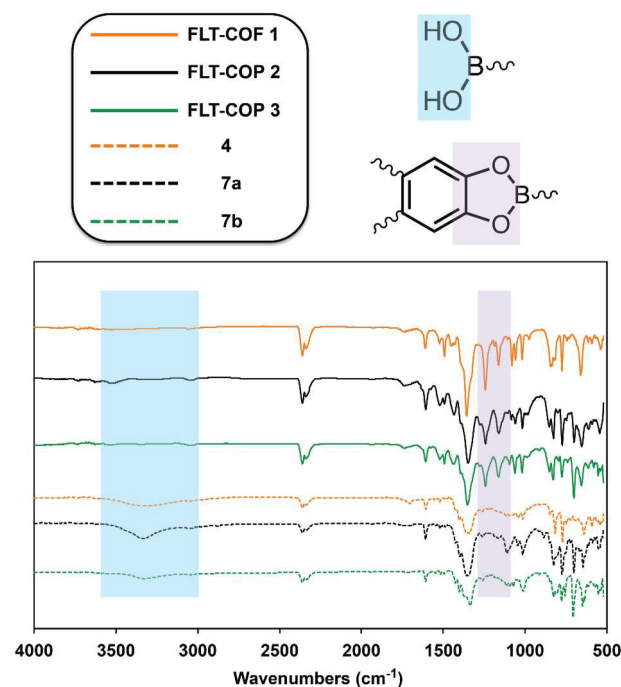


Figure 4. FT-IR spectra of FLT-COP-1 and FLT-COP-2 and -3 (solid lines) and their corresponding diboronic acid monomers (dashed lines). The relevant functional groups expected to appear (boronate esters) or disappear (boronic acids) upon COF formation are highlighted.

7a,b. Surprisingly, all three polymers showed the C–O stretching mode peak characteristic of boronate ester formation (1246 cm^{-1} for FLT-COF-1, 1244 cm^{-1} for FLT-COP-2, and 1246 cm^{-1} for FLT-COP-3) and lacked the broad OH stretch seen in each of the boronic acid monomers. This indicates that for all three polymers the boronate ester formation is occurring as expected but the crystallization step, i.e., the layer-by-layer stacking, is being disrupted in FLT-COP-2 and -3. If we consider the staggered model as an option, the diamond shaped pores in the model are approximately 10 Å between the FLT units and 20 Å between the HHTP units, which is consistent with the NLDFT data. However, as there are no discernible diffraction peaks (Figure S2), it is unlikely that this model is representative of the bulk material. It is possible, however that the sheets are randomly oriented or aggregated resulting in a small pore size distribution.

We explored the use of mixtures of FLT-COF-1 and FLT-COP-2 monomers to determine where the transition from crystalline COF to amorphous COP occurs (Figure 5). The

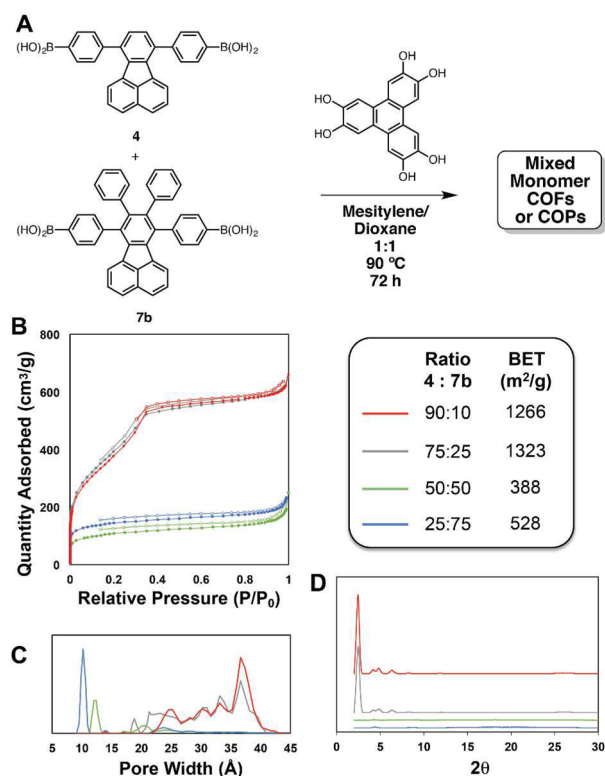


Figure 5. (A) Synthesis scheme and reaction conditions for mixed monomer COFs/COPs. (B) Nitrogen adsorption (filled circles) and desorption (open circles) isotherms (77 K) and BET surface areas of the mixed monomer FLT polymers. (C) NLDFT pore size distributions and (D) PXRD patterns of each polymer.

molar ratio between HHTP and the diboronic acid was maintained at 1:1.5, but the ratio of the diboronic acid monomers was varied as shown in Figure 5. Interestingly, there does not appear to be a gradual shift from polymers with COF-like character to amorphous COP materials. The nitrogen adsorption isotherms (Figure 5b) show that the higher molar ratios of **4** result in a type IV isotherm similar to FLT-COF-1. However, with equimolar ratios or lower, the polymer changes to a microporous material with surface areas similar to FLT-COP-2 and -3. The pore size distributions and PXRD patterns

(Figure 5c,d) also reflect this sharp transition. We hypothesize that once a critical concentration of the sterically hindered monomer **7b** is reached, the crystallization of the COF is sufficiently disrupted, leading to either an amorphous network polymer or aggregated COF-like sheets with non-ordered interlayer orientations. The staggered model shown in Figure 3 would still result in observable crystallinity by PXRD, which is not seen in FLT-COPs 2 or 3, or in the mixed monomer systems with higher fractions of monomer **7b**. Each polymer was digested in acidic deuterated dimethyl sulfoxide, and the monomer incorporation ratios were analyzed by ^1H NMR (Figure S3). These experiments confirmed that the feed ratios were representative of the monomer composition in the final polymer. This indicates that the rate of boronate ester formation is not affected by the addition of peripheral substituents.

In order to help elucidate the dramatic change between FLT-COF-1 and FLT-COP-2 and -3, MD simulations were performed (Figures 6 and 8 and Supporting Information,

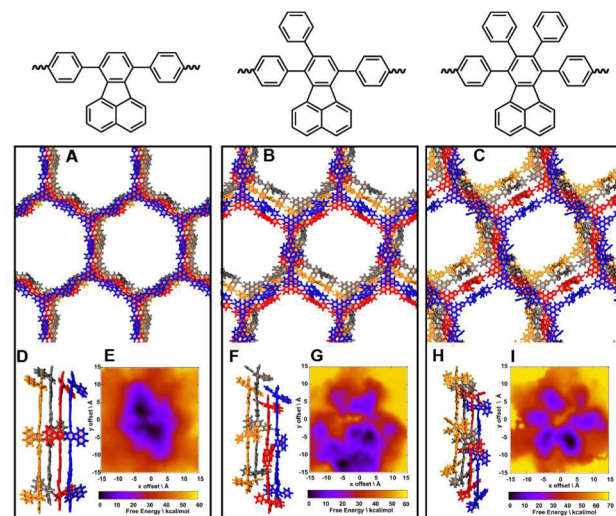


Figure 6. Molecular dynamics simulation results for three 4-layer FLT-COF/COP structures. (A, D, and E; B, F, and G; and C, H, and I represent FLT-COF-1, FLT-COP-2, and FLT-COP-3, respectively). A–C: Equilibrated COF structure, top view. D, F, H: Equilibrated COF structure, side view. E, G, I: Two dimensional free energy surface based on the x and y lateral offset of the middle two layers; the free energy minimum for each structure is assigned a value of zero. The equilibrium structures are sampled from the lowest free energy (black) regions. The bottom layer is drawn in yellow, the lower-middle layer in gray, the upper-middle layer in red, and the top layer in blue.

Figures S4 and S5). The initial condition for each of these polymers was modeled as an eclipsed COF. Four layers of each 2D extended COF structure (extended indefinitely in two dimensions through the use of hexagonal periodic boundary conditions) were constructed and subjected to two simulation protocols. First, a two-dimensional free energy landscape was obtained based on the x and y lateral offset of the middle two layers using the adaptive biasing force method (abf)¹³ as implemented in NAMD.^{14,15} Second, equilibrium simulations were run starting from the lowest free energy basin for each polymer's structure.

From Figure 6, FLT-COF-1's preference for the eclipsed conformation is clear, while FLT-COP-2 and FLT-COP-3 favor deviations from this configuration toward a staggered state.

From the equilibrium structures, it is apparent that the layers are forced to offset as more phenyl rings are added to the FLT core, disrupting well-ordered, eclipsed stacking. The side views of the FLT-COP-2 and -3 equilibrated structures shows the layers offset significantly compared to the canonically eclipsed FLT-COF-1 in which the FLT units align on top of each other. Furthermore, a detailed examination of the torsion angles around the FLT core (Figure 8) makes it clear how the extra phenyl rings disrupt the layer stacking by causing phenyl rings to orient in all three spatial dimensions, increasing the steric bulk around the FLT core in a way that cannot be accommodated in the eclipsed structure. As layers are forced to offset, favorable boron–oxygen electrostatic interactions and π -stacking interactions are disrupted. Additionally, from the two-dimensional free energy surfaces (Figure 6e,g,i), FLT-COF-1 has a distinct energy well, leading to a well-ordered crystalline structure, while FLT-COP-2 and -3 have many wells and local minima, which could be indicative of the presence of many kinetic traps that inhibit the formation of a single crystalline morphology. Detailed two- and three-dimensional representations of the free energy surfaces for each polymer are included in the Supporting Information (Figures S6–S8).

Solid-state fluorescence measurements were also carried out on both FLT-COF-1 and FLT-COP-2 and -3 and compounds 4 and 7a,b (Figure 7). Each polymer is blue-shifted (10 nm for FLT-COF-1, 15 nm for FLT-COP-2, and 25 nm for FLT-COP-3) in comparison with its corresponding boronic acid monomer. In all three examples, the polymers do not display visible fluorescence under direct irradiation with 365 nm light, whereas the diboronic acid monomers range from mildly (4) to extremely (7a,b) luminescent. This type of phenomenon has

been previously reported¹⁶ and is not completely understood. We hypothesize that the more rigidly enforced eclipsed conformation in the COF could be causing self-quenching either between FLT units themselves (in the case of FLT-COF-1) or between the FLT units and the more electron-rich HHTP monomers. This is especially apparent in the cases of FLT-COP-2 and -3, where the starting materials are very fluorescent but exhibit decreased fluorescence once polymerized into COPs. An analysis of the torsion angles obtained from the MD simulations shows that the 7 and 10 phenyl rings are affected by the addition of more phenyl rings at the 8 and 9 positions (Figure 8). The steric hindrance caused by these rings being

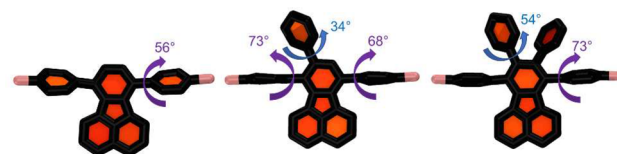


Figure 8. Average torsion angles of the 7 and 10 phenyl rings on the FLT units based on the MD simulations performed in this study. As more substituents are added, the phenyl rings are increasingly turned out of plane, with the FLT unit limiting its ability to adopt an eclipsed conformation in the solid state.

pushed further out of planarity, in combination with the added steric hindrance of the added phenyl rings may serve both to enhance the fluorescence of 7a,b in the solid state by inhibiting self-quenching and also to disrupt the formation of crystalline COF structures. The fact that there is significant interplay between the fluorescence properties and the nature of the microscopic organization of the FLT-COFs and COPs represents important information useful for the design of fluorescence sensors based on porous FLT materials in the future.

CONCLUSIONS

We have reported a novel COF and two novel COPs containing fluoranthene units with different sorption and structural properties based on the monomer's functionalization patterns. While all three polymers are porous and display narrow pore size distributions, only FLT-COF-1 possesses a mesoporous and highly ordered crystalline structure. Despite the differences in surface area and crystallinity, the boronate ester structure in all three polymers can be confirmed by IR. While the FLT units in these polymers render them luminescent, the emission is largely quenched following polymerization, owing to the enforcement of the photoactive units into arrangements where nonradiative relaxation pathways are more favorable. The presence of nonplanar aromatic rings has been shown as both an aid¹⁷ and a hindrance^{3d} to the nucleation and crystallization of COF structures. This study demonstrates the fine line between these parameters and should provide some insight into situations where the formation of crystalline COF structures *fail*. Future studies will be directed toward developing more clear and generalized design rules for how nonplanarity can affect the formation of crystalline COFs. Furthermore, we believe that the MD-based method of exploring COF structure could be useful for the design and prediction of when COFs, rather than amorphous materials, are likely to form. This method is computationally cost-effective and could be used to screen large numbers of potential COF materials prior to experimental testing.

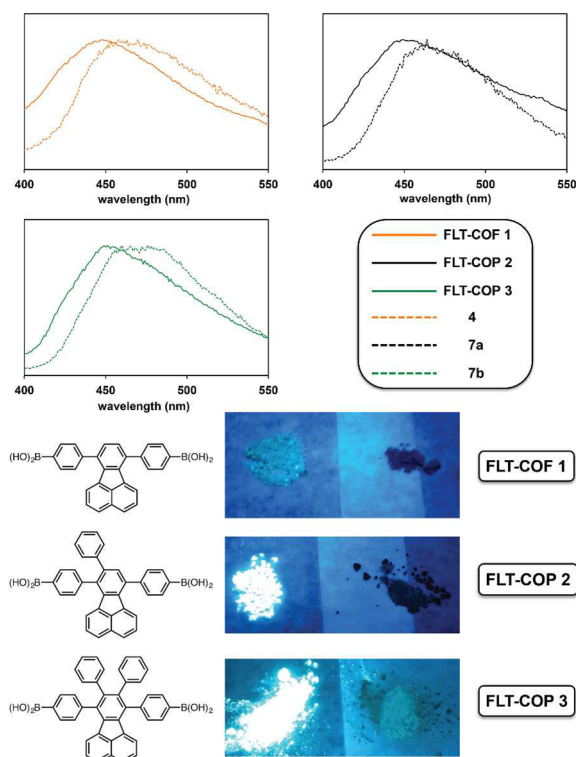


Figure 7. (Top) Solid-state fluorescence spectra of FLT-COP-1, FLT-COF-2 and -3, and boronic acids 4 and 7a,b. (Bottom) Images of each polymer and their corresponding diboronic acid monomers under long-wavelength UV irradiation.

■ EXPERIMENTAL PROCEDURES

All reagents were purchased from commercial suppliers (Sigma-Aldrich and Fisher Scientific) and used as received. HHTP was synthesized as previously reported.¹⁸ Microwave reactions were carried out in a CEM Discover reactor. Fluorescence measurements were carried out on a Horiba Fluorolog spectrophotometer. FT-IR spectra were taken on an Agilent Technologies Cary 600 series instrument. Thermogravimetric analyses were performed using a Mettler Toledo DSC/TGA 1 under nitrogen atmosphere with a heating rate of 10 °C h⁻¹ from 25–800 °C. Low-pressure gas adsorption experiments (up to 760 Torr) were carried out on a Micromeritics ASAP 2020 surface area analyzer. Ultrahigh-purity-grade N₂ and He gases (obtained from Airgas Corp.) were used in all adsorption measurements. N₂ isotherms were measured using a liquid nitrogen bath (77 K). Pore size distributions were determined using an NLDFT carbon slit-pore model in the Micromeritics Software Package. Powder X-ray diffraction of the FLT polymers was carried out on a Bruker D8 Advance diffractometer with a sealed tube radiation source (Cu K α , λ = 1.54184 Å), low background sample holder, and Lynxeye XE detector. Data were collected over a 2 θ range of 2–30° in Bragg–Brentano geometry with generator settings of 40 kV and 30 mA, step size of 0.02°, and exposure time per step of 2 s.

Monomer and Polymer Synthesis. 1: To a round-bottom flask containing 1,3-bis(4-bromophenyl)-2-propanone (2 g, 5.4 mmol) was added acenaphthenequinone (1.1 g, 6.04 mmol). This was dissolved into CH₂Cl₂ (5 mL), and then MeOH (30 mL) was added. To this mixture was added KOH (160 mg, 2.7 mmol), and the reaction was heated to reflux for 2 h. After that time the reaction was cooled to room temperature and filtered to yield a dark purple solid (2.49 g, 90%). Spectra matched those previously reported in the literature.^{9b}

2: To a round-bottom flask containing **1** (2.00 g, 3.9 mmol) and norbornadiene (15 mL, 147 mmol) was added acetic anhydride (20 mL). The solution was refluxed at 140 °C for 7 d. The solution was cooled to room temperature. The resulting solid was filtered out and washed with methanol to give **2** (1.529 g, 77%). Spectra matched literature values.¹⁹

3: To a seal tube containing **2** (500 mg, 0.98 mmol) was added B₂Pin₂ (546 mg, 2.2 mmol) followed by KOAc (963 mg, 9.8 mmol). This was dissolved into dioxane (5 mL) and degassed under N₂ for 15 min. After that time Pd(dppf) (129 mg, 0.15 mmol) was added, and the tube was sealed with a Teflon cap before being heated to 100 °C for 72 h. The reaction was then cooled to room temperature and poured into MeOH (50 mL). The resulting precipitate was filtered and washed with MeOH (20 mL), resulting in pure material (526 mg, 88%). ¹H NMR (400 MHz, DMSO, ppm): δ 8.05 (d, 4H, J = 7.6 Hz), 7.75 (d, 2H, J = 7.9 Hz), 7.69 (d, 4H, J = 7.6 Hz), 7.35 (t, 2H, J = 7.5), 7.3 (m, 4H), 1.4 (s, 24H). ¹³C NMR (500 MHz, CDCl₃, ppm): δ 143.9, 137.9, 136.7, 136.1, 135.0, 132.7, 129.8, 129.0, 128.5, 127.6, 126.8, 123.2, 84.0, 25.0. MS (ESI⁺) calcd for C₄₀H₄₀O₄B₂: 607.3199, found: 607.3183 [M + H]⁺.

4: To a round-bottom flask containing **3** (500 mg, 0.825 mmol) was added NaIO₄ (2.28 g, 10.7 mmol). This was dissolved in a solution of 3:1:1 THF:H₂O:EtOAc (15 mL) before being heated to reflux for 24 h. After that time the reaction was cooled to room temperature, and 1 M HCl (10 mL) was added. The reaction was then allowed to stir at room temperature for a further 24 h before being poured into water (50 mL). The resulting precipitate was washed with more water (20 mL) before being air-dried on the filter. This material did not require further purification. (302 mg, 83%). ¹H NMR (400 MHz, DMSO, ppm): δ 8.2 (s, 4H), 8.05 (d, 4H, J = 6.7 Hz), 7.9 (d, 2H, J = 7.0 Hz), 7.6 (d, 4H, J = 7.0 Hz), 7.48 (t, 2H, J = 7.0 Hz), 7.3 (s, 2H), 7.2 (d, 2H, J = 6.8 Hz). ¹³C NMR (500 MHz, CDCl₃, ppm): δ 142.2, 138.2, 136.3, 135.8, 135.1, 132.3, 130.0, 129.6, 128.3, 128.2, 127.6, 123.2. MALDI-ToF-MS (m/z) calcd for [C₂₈H₂₀B₂O₄]⁺: 442.15, found: 442.72.

5a: To a microwave vial containing **1** (500 mg, 0.97 mmol) and phenyl acetylene (0.11 mL, 0.97 mmol) was added diphenyl ether (1 mL). This was then microwaved for 2 h at 250 °C and 300 W. After that time an orange solid was filtered, washed with hexanes (5 mL)

and methanol (10 mL), and dried under vacuum to give the desired product as an orange solid (515 mg, 89%). Spectra matched literature values.^{9a}

5b: To a microwave vial containing **1** (700 mg, 1.5 mmol) and diphenyl acetylene (282 mg, 1.4 mmol) was added diphenyl ether (1 mL). This was then heated using microwave irradiation for 2 h at 250 °C and 300 W. An orange solid was filtered, washed with hexanes (5 mL) and methanol (20 mL), and dried under vacuum to give the desired product without further purification (770 mg, 85%). Spectra matched literature values.^{9b}

6a: To a seal tube containing **5a** (500 mg, 0.85 mmol) was added B₂Pin₂ (476 mg, 1.9 mmol) followed by KOAc (837 mg, 8.5 mmol). This was dissolved into dioxane (5 mL) and degassed under N₂ for 15 min. After that time Pd(dppf) (105 mg, 0.15 mmol) was added, and the tube was sealed with a Teflon cap before being heated to 110 °C for 72 h. The reaction was then cooled to room temperature and poured into MeOH (50 mL). The resulting precipitate was filtered and washed with MeOH (20 mL), resulting in pure material (430 mg, 74%). ¹H NMR (400 MHz, DMSO, ppm): δ 8.02 (d, 2H, J = 7.5 Hz), 7.85 (d, 2H, J = 7.5 Hz), 7.8–7.7 (m, 4H), 7.45–7.35 (m, 4H), 7.35–7.3 (m, 2H), 7.25–7.15 (m, 4H), 6.7 (d, 2H, J = 7.0 Hz), 1.4 (s, 24H). ¹³C NMR (500 MHz, CDCl₃, ppm): δ 143.7, 142.4, 140.9, 140.6, 138.1, 137.8, 136.4, 136.2, 135.7, 135.6, 135.1, 134.8, 133.1, 131.0, 129.9, 129.8, 129.7, 128.6, 127.7, 127.6, 127.5, 126.68, 126.66, 126.4, 123.6, 123.1, 84.0, 83.9, 25.00, 24.98. MS (ESI⁺) calcd for C₄₆H₄₄O₄B₂: 705.3333, found: 705.3322 [M + Na]⁺.

6b: To a seal tube containing **5b** (500 mg, 0.75 mmol) was added B₂Pin₂ (422 mg, 1.7 mmol) followed by KOAc (741 mg, 7.6 mmol). This was dissolved into dioxane (5 mL) and degassed under N₂ for 15 min. After that time Pd(dppf) (93 mg, 0.11 mmol) was added, and the tube was sealed with a Teflon cap before being heated to 110 °C for 72 h. The reaction was then cooled to room temperature and poured into MeOH (50 mL). The resulting precipitate was filtered and washed with MeOH (20 mL) resulting in pure material (453 mg, 83%). ¹H NMR (400 MHz, DMSO, ppm): δ 7.75 (d, 4H, J = 7.5 Hz), 7.7 (d, 2H, J = 8.2 Hz), 7.35 (d, 4H, J = 7.5 Hz), 7.3 (t, 2H, J = 7.8 Hz), 7.0–6.8 (m, 10H), 6.6 (d, 2H, J = 7.0 Hz), 1.4 (s, 24H). ¹³C NMR (500 MHz, CDCl₃, ppm): δ 142.9, 140.5, 139.6, 137.1, 136.4, 136.2, 134.6, 133.2, 131.2, 129.54, 129.51, 127.7, 126.7, 126.5, 125.4, 123.4, 84.0, 24.8. MS (ESI⁺) calcd for C₅₂H₄₈O₄B₂: 797.3387, found: 797.3376 [M + K]⁺.

7a: To a round-bottom flask containing **6a** (147 mg, 0.22 mmol) was added NaIO₄ (600 mg, 2.8 mmol). This was dissolved in a 3:1:1 THF:H₂O:EtOAc mixture (5 mL) before being heated to reflux for 24 h. After this time the reaction was cooled to room temperature, and 1 M HCl (10 mL) was added. The reaction was then allowed to stir at room temperature for a further 24 h before being poured into water (50 mL). The resulting precipitate was washed with a more water (20 mL) before being air-dried on the filter, resulting in pure material. (95 mg, 85%). ¹H NMR (400 MHz, DMSO, ppm): δ 8.2 (s, 2H), 8.15 (s, 2H), 8.0 (d, 2H, J = 7.9 Hz), 7.86–7.82 (m, 4H), 7.65 (d, 2H, J = 7.9 Hz), 7.45 (t, 1H, J = 7.6 Hz), 7.38 (t, 1H, J = 7.6 Hz), 7.35 (d, 2H, J = 7.9 Hz), 7.3–7.15 (m, 7H), 6.5 (d, 1H, J = 7.1 Hz). ¹³C NMR (400 MHz, CDCl₃, ppm): δ 141.9, 140.90, 140.86, 140.82, 138.2, 138.0, 135.6, 136.2, 135.5, 135.1, 135.0, 134.9, 132.7, 131.2, 130.1, 130.0, 129.4, 128.3, 128.2, 127.6, 127.1, 123.4, 123.1. MALDI-ToF-MS (m/z) calcd for [C₃₄H₂₄B₂O₄]⁺: 518.19, found: 518.72.

7b: To a round-bottom flask containing **6b** (493 mg, 0.65 mmol) was added NaIO₄ (1.8 g, 8.4 mmol). This was dissolved in a THF:H₂O:EtOAc mixture (3:1:1 by vol, 15 mL) before being heated to reflux for 24 h. After this time the reaction was cooled to room temperature, and 1 M HCl (10 mL) was added. The reaction was then allowed to stir at room temperature for a further 24 h before being poured into water (50 mL). The resulting precipitate was washed with a more water (20 mL) before being air-dried on the filter, resulting in pure material. (313 mg, 81% yield). ¹H NMR (400 MHz, DMSO, ppm): δ 8.1 (s, 4H), 7.85 (d, 2H, J = 8.2 Hz), 7.75 (d, 4H, J = 7.9 Hz), 7.35 (t, 2H, J = 7.5 Hz), 7.3 (d, 4H, J = 7.9 Hz), 7.0 (m, 4H), 6.9 (t, 4H, J = 7.3 Hz), 6.85 (t, 2H, J = 7.2 Hz), 6.4 (d, 2H, J = 7.1 Hz). ¹³C NMR (500 MHz, CDCl₃, ppm): δ 141.5, 140.8, 139.8, 137.4, 136.1,

136.0, 134.6, 132.8, 131.3, 129.8, 129.1, 128.3, 127.4, 127.0, 126.1, 123.2. MALDI-ToF-MS (m/z) calcd for $[C_{40}H_{28}B_2O_4]^+$: 594.22, found: 594.74.

FLT-COF-1: To a vial containing HHTP (14.7 mg, 0.045 mmol) fully dissolved in dioxane (4 mL) was added **4** (30 mg, 0.068 mmol). To this was added mesitylene (4 mL), and the vial was capped and heated at 90 °C for 72 h. After that time, the resulting powder was filtered and washed with dry toluene (1 mL) before being collected by filtration and dried under dynamic vacuum at 120 °C for 12 h. (27.9 mg, 40%).

FLT-COP-2: To a vial containing HHTP (12.5 mg, 0.038 mmol) fully dissolved in dioxane (4 mL) was added **7a** (30 mg, 0.058 mmol). To this was added mesitylene (4 mL), and the vial was capped and heated at 90 °C for 72 h. After that time, the resulting powder was filtered and washed with dry toluene (1 mL) before being collected by filtration and dried under dynamic vacuum at 120 °C for 12 h. (18.0 mg, 38%).

FLT-COP-3: To a vial containing HHTP (11 mg, 0.034 mmol) fully dissolved in dioxane (4 mL) was added **7b** (30 mg, 0.050 mmol). To this was added mesitylene (4 mL), and the vial was capped and heated at 90 °C for 72 h. After that time, the resulting powder was filtered and washed with dry toluene (1 mL) before being collected by filtration and dried under dynamic vacuum at 120 °C for 12 h. (22.6 mg, 38%).

Computational Methods. The MD simulations used a fully atomistic force field which was obtained from a combination of cgenff²⁰ and prior literature on similar COFs²¹ (see [Supporting Information](#), Figure S4, for full details). A fragment of the 2D structure shown in [Figure 1](#) was generated, and boronate ester bonds were applied across the unit cell boundary to produce an infinitely extended 2D structure. Then four of these 2D structures were stacked in the z -direction to generate a four-layer stack. The hexagonal unit cell used for all three COF/COP types was as follows: cellbasisvector1 47.0 0.0 0.0, cellbasisvector2 23.5 40.7 0.0, and cellbasisvector3 0.0 0.0 200.0. The numbers of total atoms in the unit cell are as follow: FLT-COF-1, 792; FLT-COP-2, 912; and FLT-COP-3, 1032 (for the four-layer stack). This small system size makes the MD simulations very efficient; in fact, they can all be run to completion on a laptop computer within a few days. We used the NAMD software package¹⁵ with the following parameter choices: temperature 363 K (enforced with a Langevin thermostat with damping parameter 1.0 ps⁻¹; cutoff distance 12 Å (for the van der Waals interactions and the changeover from real space to inverse space for the electrostatic interactions); time step 1.0 fs; particle mesh Ewald grid spacing of 1.0 Å. For the free energy simulations, we used the adaptive biasing force method¹³ in two dimensions based on the x and y lateral offset of the middle two stacked layers. We used a grid spacing of 0.4 Å in each direction. In addition the outer two layers were not allowed to separate by more than 12 Å to keep the four layer stack intact. The free energy converges after about 2×10^8 time steps. Structures corresponding to the minimum free energy basin for each polymer were extracted from the free energy runs and used to initiate equilibrium simulations free from any biasing forces. These simulations were used to generate representative snapshots for [Figure 6](#). Images were generated using the VMD software package.²²

■ ASSOCIATED CONTENT

● Supporting Information

The Supporting Information is available free of charge on the ACS Publications website at DOI: 10.1021/jacs.7b05555.

Thermogravimetric analysis, fractional coordinates for the simulated COF models, and MD simulations (PDF)

■ AUTHOR INFORMATION

Corresponding Authors

*steven.nielsen@utdallas.edu

*ronald.smaldone@utdallas.edu

ORCID

Ronald A. Smaldone: 0000-0003-4560-7079

Author Contributions

*C.M.T. and G.O. contributed equally.

Notes

The authors declare no competing financial interest.

■ ACKNOWLEDGMENTS

This research was supported with funds from the University of Texas at Dallas and the American Chemical Society Petroleum Research Fund (52906-DNI10).

■ REFERENCES

- (1) (a) Cote, A. P.; Benin, A. I.; Ockwig, N. W.; O'Keeffe, M.; Matzger, A. J.; Yaghi, O. M. *Science* **2005**, 310, 1166. (b) El-Kaderi, H. M.; Hunt, J. R.; Mendoza-Cortés, J. L.; Côté, A. P.; Taylor, R. E.; O'Keeffe, M.; Yaghi, O. M. *Science* **2007**, 316, 268. (c) Colson, J. W.; Dichtel, W. R. *Nat. Chem.* **2013**, 5, 453. (d) Waller, P. J.; Gándara, F.; Yaghi, O. M. *Acc. Chem. Res.* **2015**, 48, 3053. (e) DeBlase, C. R.; Dichtel, W. R. *Macromolecules* **2016**, 49, 5297. (f) Jiang, J.; Zhao, Y.; Yaghi, O. M. *J. Am. Chem. Soc.* **2016**, 138, 3255. (g) Alahakoon, S. B.; Thompson, C. M.; Occhialini, G.; Smaldone, R. A. *ChemSusChem* **2017**, 10, 2116.
- (2) (a) Ganz, E.; Dornfeld, M. *J. Phys. Chem. C* **2012**, 116, 3661. (b) Rabbani, M. G.; Sekizkardes, A. K.; Kahveci, Z.; Reich, T. E.; Ding, R.; El-Kaderi, H. M. *Chem. - Eur. J.* **2013**, 19, 3324. (c) Huang, N.; Chen, X.; Krishna, R.; Jiang, D. *Angew. Chem., Int. Ed.* **2015**, 54, 2986. (d) DeBlase, C. R.; Hernández-Burgos, K.; Silberstein, K. E.; Rodríguez-Calero, G. G.; Bisbey, R. P.; Abruña, H. D.; Dichtel, W. R. *ACS Nano* **2015**, 9, 3178. (e) Lu, H.; Wang, C.; Chen, J.; Ge, R.; Leng, W.; Dong, B.; Huang, J.; Gao, Y. *Chem. Commun.* **2015**, 51, 15562. (f) Stegbauer, L.; Hahn, M. W.; Jentys, A.; Savasci, G.; Ochsenfeld, C.; Lercher, J. A.; Lotsch, B. V. *Chem. Mater.* **2015**, 27, 7874. (g) Alahakoon, S. B.; Thompson, C. M.; Nguyen, A. X.; Occhialini, G.; McCandless, G. T.; Smaldone, R. A. *Chem. Commun.* **2016**, 52, 2843. (h) Zeng, Y.; Zou, R.; Zhao, Y. *Adv. Mater.* **2016**, 28, 2855. (i) Pyles, D. A.; Crowe, J. W.; Baldwin, L. A.; McGrier, P. L. *ACS Macro Lett.* **2016**, 5, 1055.
- (3) (a) Pachfule, P.; Kandambeth, S.; Diaz Diaz, D.; Banerjee, R. *Chem. Commun.* **2014**, 50, 3169. (b) Stegbauer, L.; Schwinghammer, K.; Lotsch, B. V. *Chem. Sci.* **2014**, 5, 2789. (c) Lin, S.; Diercks, C. S.; Zhang, Y.-B.; Kornienko, N.; Nichols, E. M.; Zhao, Y.; Paris, A. R.; Kim, D.; Yang, P.; Yaghi, O. M.; Chang, C. J. *Science* **2015**, 349, 1208. (d) Vyas, V. S.; Haase, F.; Stegbauer, L.; Savasci, G.; Podjaski, F.; Ochsenfeld, C.; Lotsch, B. V. *Nat. Commun.* **2015**, 6, 8508. (e) Xu, H.; Gao, J.; Jiang, D. *Nat. Chem.* **2015**, 7, 905.
- (4) (a) DeBlase, C. R.; Silberstein, K. E.; Truong, T.-T.; Abruña, H. D.; Dichtel, W. R. *J. Am. Chem. Soc.* **2013**, 135, 16821. (b) Zha, Z.; Xu, L.; Wang, Z.; Li, X.; Pan, Q.; Hu, P.; Lei, S. *ACS Appl. Mater. Interfaces* **2015**, 7, 17837. (c) Vazquez-Molina, D. A.; Mohammad-Pour, G. S.; Lee, C.; Logan, M. W.; Duan, X.; Harper, J. K.; Uribe-Romo, F. J. *J. Am. Chem. Soc.* **2016**, 138, 9767.
- (5) (a) Crowe, J. W.; Baldwin, L. A.; McGrier, P. L. *J. Am. Chem. Soc.* **2016**, 138, 10120. (b) Dalapati, S.; Jin, E.; Addicoat, M.; Heine, T.; Jiang, D. *J. Am. Chem. Soc.* **2016**, 138, 5797. (c) Dalapati, S.; Gu, C.; Jiang, D. *Small* **2016**, 12, 6513–6527.
- (6) (a) Bunck, D. N.; Dichtel, W. R. *J. Am. Chem. Soc.* **2013**, 135, 14952. (b) Chen, X.; Addicoat, M.; Irle, S.; Nagai, A.; Jiang, D. *J. Am. Chem. Soc.* **2013**, 135, 546. (c) Smith, B. J.; Dichtel, W. R. *J. Am. Chem. Soc.* **2014**, 136, 8783. (d) Smith, B. J.; Hwang, N.; Chavez, A. D.; Novotney, J. L.; Dichtel, W. R. *Chem. Commun.* **2015**, 51, 7532. (e) Smith, B. J.; Overholts, A. C.; Hwang, N.; Dichtel, W. R. *Chem. Commun.* **2016**, 52, 3690.
- (7) Chen, X.; Addicoat, M.; Jin, E.; Zhai, L.; Xu, H.; Huang, N.; Guo, Z.; Liu, L.; Irle, S.; Jiang, D. *J. Am. Chem. Soc.* **2015**, 137, 3241.
- (8) Sygula, A.; Rabideau, P. W. *J. Am. Chem. Soc.* **1999**, 121, 7800.

- (9) (a) Venkatramaiah, N.; Kumar, S.; Patil, S. *Chem. Commun.* **2012**, 48, 5007. (b) Kumar, S.; Venkatramaiah, N.; Patil, S. *J. Phys. Chem. C* **2013**, 117, 7236. (c) Kumar, S.; Kumar, D.; Patil, Y.; Patil, S. *J. Mater. Chem. C* **2016**, 4, 193.
- (10) Spitler, E. L.; Koo, B. T.; Novotney, J. L.; Colson, J. W.; Uribe-Romo, F. J.; Gutierrez, G. D.; Clancy, P.; Dichtel, W. R. *J. Am. Chem. Soc.* **2011**, 133, 19416.
- (11) (a) Das, G.; Biswal, B. P.; Kandambeth, S.; Venkatesh, V.; Kaur, G.; Addicoat, M.; Heine, T.; Verma, S.; Banerjee, R. *Chem. Sci.* **2015**, 6, 3931. (b) Mitra, S.; Kandambeth, S.; Biswal, B. P.; Khayum M, A.; Choudhury, C. K.; Mehta, M.; Kaur, G.; Banerjee, S.; Prabhune, A.; Verma, S.; Roy, S.; Kharul, U. K.; Banerjee, R. *J. Am. Chem. Soc.* **2016**, 138, 2823.
- (12) Smith, M. K.; Northrop, B. H. *Chem. Mater.* **2014**, 26, 3781.
- (13) (a) Darve, E.; Rodríguez-Gómez, D.; Pohorille, A. *J. Chem. Phys.* **2008**, 128, 144120. (b) Hénin, J.; Fiorin, G.; Chipot, C.; Klein, M. L. *J. Chem. Theory Comput.* **2010**, 6, 35.
- (14) NAMD was developed by the Theoretical and Computational Biophysics Group in the Beckman Institute for Advanced Science and Technology at the University of Illinois at Urbana–Champaign.
- (15) Phillips, J. C.; Braun, R.; Wang, W.; Gumbart, J.; Tajkhorshid, E.; Villa, E.; Chipot, C.; Skeel, R. D.; Kalé, L.; Schulten, K. *J. Comput. Chem.* **2005**, 26, 1781.
- (16) Baldwin, L. A.; Crowe, J. W.; Shannon, M. D.; Jaroniec, C. P.; McGrier, P. L. *Chem. Mater.* **2015**, 27, 6169.
- (17) Ascherl, L.; Sick, T.; Margraf, J. T.; Lapidus, S. H.; Calik, M.; Hettstedt, C.; Karaghiosoff, K.; Döblinger, M.; Clark, T.; Chapman, K. W.; Auras, F.; Bein, T. *Nat. Chem.* **2016**, 8, 310.
- (18) Percec, V.; Imam, M. R.; Peterca, M.; Wilson, D. A.; Graf, R.; Spiess, H. W.; Balagurusamy, V. S. K.; Heiney, P. A. *J. Am. Chem. Soc.* **2009**, 131, 7662.
- (19) Plummer, B. F.; Steffen, L. K.; Braley, T. L.; Reese, W. G.; Zych, K.; Van Dyke, G.; Tulley, B. *J. Am. Chem. Soc.* **1993**, 115, 11542.
- (20) (a) Vanommeslaeghe, K.; MacKerell, A. D. *J. Chem. Inf. Model.* **2012**, 52, 3144. (b) Vanommeslaeghe, K.; Raman, E. P.; MacKerell, A. D. *J. Chem. Inf. Model.* **2012**, 52, 3155.
- (21) (a) Amirjalayer, S.; Snurr, R. Q.; Schmid, R. *J. Phys. Chem. C* **2012**, 116, 4921. (b) Koo, B. T.; Heden, R. F.; Clancy, P. *Phys. Chem. Chem. Phys.* **2017**, 19, 9745.
- (22) Humphrey, W.; Dalke, A.; Schulten, K. *J. Mol. Graphics* **1996**, 14, 33.